

# UC Riverside

## UC Riverside Previously Published Works

### Title

Random laser imaging of bovine pericardium under the uniaxial tensile test.

### Permalink

<https://escholarship.org/uc/item/57q1t48m>

### Journal

Biomedical Optics Express, 9(8)

### ISSN

2156-7085

### Authors

Cuando-Espitia, Natanael  
Sánchez-Arévalo, Francisco  
Hernández-Cordero, Juan

### Publication Date

2018-08-01

### DOI

10.1364/boe.9.003523

### Copyright Information

This work is made available under the terms of a Creative Commons Attribution License, available at <https://creativecommons.org/licenses/by/4.0/>

Peer reviewed



# Random laser imaging of bovine pericardium under the uniaxial tensile test

NATANAEL CUANDO-ESPITIA,<sup>1</sup> FRANCISCO SÁNCHEZ-ARÉVALO,<sup>2</sup> AND JUAN HERNÁNDEZ-CORDERO<sup>2,\*</sup>

<sup>1</sup>Department of Mechanical Engineering, University of California Riverside, Riverside, CA 92521, USA

<sup>2</sup>Instituto de Investigaciones en Materiales, Universidad Nacional Autónoma de México, A.P. 70-360, Cd. Universitaria, México D.F. 04510, México

\*[jhcordero@iim.unam.mx](mailto:jhcordero@iim.unam.mx)

**Abstract:** We demonstrate random laser (RL) emission from within bovine pericardium (BP) tissue. The interest in BP relies on its wide use as a valve replacement and as a biological patch. By imaging the emitting tissue, we show that RL emission is mostly generated inside the collagen fibers. Multimode RL operation is thus achieved within the volume of each fiber. Image analysis reveals that the intensity of the RL emission from individual fibers is dependent on the relative orientation to the stress axis. Our results suggest that RL intensity may be used as an indicator of stress concentration in individual fibers.

© 2018 Optical Society of America under the terms of the [OSA Open Access Publishing Agreement](#)

**OCIS codes:** (170.0170) Medical optics and biotechnology; (170.0110) Imaging systems; (170.6935) Tissue characterization.

## References and links

1. E. J. Benjamin, S. S. Virani, C. W. Callaway, A. M. Chamberlain, A. R. Chang, S. Cheng, S. E. Chiuve, M. Cushman, F. N. Delling, R. Deo, S. D. de Ferranti, J. F. Ferguson, M. Fornage, C. Gillespie, C. R. Isasi, M. C. Jiménez, L. C. Jordan, S. E. Judd, D. Lackland, J. H. Lichtman, L. Lisabeth, S. Liu, C. T. Longenecker, P. L. Lutsey, J. S. Mackey, D. B. Matchar, K. Matsushita, M. E. Mussolino, K. Nasir, M. O'Flaherty, L. P. Palaniappan, A. Pandey, D. K. Pandey, M. J. Reeves, M. D. Ritchey, C. J. Rodriguez, G. A. Roth, W. D. Rosamond, U. K. A. Sampson, G. M. Satou, S. H. Shah, N. L. Spartano, D. L. Tirschwell, C. W. Tsao, J. H. Voeks, J. Z. Willey, J. T. Wilkins, J. H. Wu, H. M. Alger, S. S. Wong, and P. Muntner; American Heart Association Council on Epidemiology and Prevention Statistics Committee and Stroke Statistics Subcommittee, "Heart disease and stroke statistics-2018 update: a report from the American Heart Association," *Circulation* **137**(12), e67–e492 (2018).
2. L. Søndergaard, A. Saraste, C. Christersson, and A. Vahanian, "The year in cardiology 2017: valvular heart disease," *Eur. Heart J.* **39**(8), 650–657 (2018).
3. M. L. Brown, H. V. Schaff, B. D. Lahr, C. J. Mullany, T. M. Sundt, J. A. Dearani, C. G. McGregor, and T. A. Orszulak, "Aortic valve replacement in patients aged 50 to 70 years: improved outcome with mechanical versus biologic prostheses," *J. Thorac. Cardiovasc. Surg.* **135**(4), 878–884 (2008).
4. K. Hammermeister, G. K. Sethi, W. G. Henderson, F. L. Grover, C. Oprian, and S. H. Rahimtoola, "Outcomes 15 years after valve replacement with a mechanical versus a bioprosthetic valve: final report of the Veterans Affairs randomized trial," *J. Am. Coll. Cardiol.* **36**(4), 1152–1158 (2000).
5. L. P. Dasi, J. Grande-Allen, K. Kunzelman, and E. Kuhl, "The pursuit of engineering the ideal heart valve replacement or repair: a special issue of the annals of biomedical engineering," *Ann. Biomed. Eng.* **45**(2), 307–309 (2017).
6. A. Karimi, S. M. Rahmati, T. Sera, S. Kudo, and M. Navidbakhsh, "A combination of experimental and numerical methods to investigate the role of strain rate on the mechanical properties and collagen fiber orientations of the healthy and atherosclerotic human coronary arteries," *Bioengineered* **8**(2), 154–170 (2017).
7. P. Fratzl, *Collagen: Structure and Mechanics* (Springer, 2008).
8. V. R. Sherman, W. Yang, and M. A. Meyers, "The materials science of collagen," *J. Mech. Behav. Biomed. Mater.* **52**, 22–50 (2015).
9. M. S. Sacks, C. J. Chuong, and R. More, "Collagen fiber architecture of bovine pericardium," *ASAIO J.* **40**(3), M632–M637 (1994).
10. T. Boulesteix, A. M. Pena, N. Pagès, G. Godeau, M. P. Sauviat, E. Beaurepaire, and M. C. Schanne-Klein, "Micrometer scale ex vivo multiphoton imaging of unstained arterial wall structure," *Cytometry A* **69A**(1), 20–26 (2006).
11. N. Cuando-Espitia, F. Sánchez-Arévalo, and J. Hernández-Cordero, "Mechanical assessment of bovine pericardium using Mueller matrix imaging, enhanced backscattering and digital image correlation analysis," *Biomed. Opt. Express* **6**(8), 2953–2960 (2015).

12. S. H. Alavi, V. Ruiz, T. Krasieva, E. L. Botvinick, and A. Kheradvar, "Characterizing the collagen fiber orientation in pericardial leaflets under mechanical loading conditions," *Ann. Biomed. Eng.* **41**(3), 547–561 (2013).
13. T. F. Bartsch, M. D. Kochanczyk, E. N. Lissek, J. R. Lange, and E. L. Florin, "Nanoscope Imaging of Thick Heterogeneous Soft-Matter Structures in Aqueous Solution," *Nat. Commun.* **7**, 12729 (2016).
14. H. Cao, Y. G. Zhao, S. T. Ho, E. W. Seelig, Q. H. Wang, and R. P. H. Chang, "Random Laser Action in Semiconductor Powder," *Phys. Rev. Lett.* **82**(11), 2278–2281 (1999).
15. C. R. Lee, S. H. Lin, C. H. Guo, S. H. Chang, T. S. Mo, and S. C. Chu, "All-optically controllable random laser based on a dye-doped polymer-dispersed liquid crystal with nano-sized droplets," *Opt. Express* **18**(3), 2406–2412 (2010).
16. Y. L. Chen, C. L. Chen, H. Y. Lin, C. W. Chen, Y. F. Chen, Y. Hung, and C. Y. Mou, "Enhancement of random lasing based on the composite consisting of nanospheres embedded in nanorods template," *Opt. Express* **17**(15), 12706–12713 (2009).
17. R. C. Polson and Z. V. Vardeny, "Random lasing in human tissues," *Appl. Phys. Lett.* **85**(7), 1289–1291 (2004).
18. Q. Song, Z. Xu, S. H. Choi, X. Sun, S. Xiao, O. Akkus, and Y. L. Kim, "Detection of nanoscale structural changes in bone using random lasers," *Opt. Lett.* **35**(15), 2624–2626 (2010).
19. E. Shojaie and K. Madanipour, "Detection of nanoparticle changes in nanocomposite active sample using random laser emission," *Proc. SPIE* **10330**, 103301L (2017).
20. S. H. Choi and Y. L. Kim, "Random lasing alterations by single-nanoparticle perturbations," *Appl. Phys. Lett.* **100**(4), 041101 (2012).
21. J. C. Briones-Herrera, N. Cuando-Espitia, F. M. Sánchez-Arévalo, and J. Hernández-Cordero, "Evaluation of mechanical behavior of soft tissue by means of random laser emission," *Rev. Sci. Instrum.* **84**(10), 104301 (2013).
22. D. S. Wiersma, "Random lasers explained," *Nat. Photonics* **3**(5), 246–247 (2009).
23. F. M. Sánchez-Arévalo, M. Farfán, D. Covarrubias, R. Zenit, and G. Pulos, "The micromechanical behavior of lyophilized glutaraldehyde-treated bovine pericardium under uniaxial tension," *J. Mech. Behav. Biomed. Mater.* **3**(8), 640–646 (2010).
24. C. E. Willert and M. Gharib, "Digital particle image velocimetry," *Exp. Fluids* **10**(4), 181–193 (1991).
25. F. M. Sánchez-Arévalo and G. Pulos, "Use of digital image correlation to determine the mechanical behavior of materials," *Mater. Charact.* **59**(11), 1572–1579 (2008).
26. F. M. Sánchez-Arévalo, T. García-Fernández, G. Pulos, and M. Villagrán-Muniz, "Use of digital speckle pattern correlation for strain measurements in a CuAlBe shape memory alloy," *Mater. Charact.* **60**(8), 775–782 (2009).
27. F. Tenopala-Carmona, C. García-Segundo, N. Cuando-Espitia, and J. Hernández-Cordero, "Angular distribution of random laser emission," *Opt. Lett.* **39**(3), 655–658 (2014).
28. A. Mikhail, Noginov, *Solid-state Random Lasers* (Springer, 2005).
29. F. Yuan-Cheng, *Biomechanics: Properties of Living Tissues* (Springer, 2013).
30. J. Andeasen, A. A. Asatryan, L. C. Botten, M. A. Byrne, H. Cao, L. Ge, L. Labonté, P. Sebahh, A. D. Stone, H. E. Türeci, and C. Vanneste, "Modes of random lasers," *Adv. Opt. Photonics* **3**(1), 88–127 (2011).
31. J. T. C. Schrauwen, A. Vilanova, R. Rezakhaniha, N. Stergiopoulos, F. N. van de Vosse, and P. H. M. Bovendeerd, "A method for the quantification of the pressure dependent 3D collagen configuration in the arterial adventitia," *J. Struct. Biol.* **180**(2), 335–342 (2012).
32. R. M. Williams, W. R. Zipfel, and W. W. Webb, "Interpreting second-harmonic generation images of collagen I fibrils," *Biophys. J.* **88**(2), 1377–1386 (2005).
33. I. Gusachenko, V. Tran, Y. Goulam Houssen, J.-M. Allain, and M.-C. Schanne-Klein, "Polarization-resolved second-harmonic generation in tendon upon mechanical stretching," *Biophys. J.* **102**(9), 2220–2229 (2012).
34. A. Fiorani, C. Gualandi, S. Panseri, M. Montesi, M. Marcacci, M. L. Focarete, and A. Bigi, "Comparative performance of collagen nanofibers electrospun from different solvents and stabilized by different crosslinkers," *J. Mater. Sci. Mater. Med.* **25**(10), 2313–2321 (2014).
35. F. Schaff, M. Bech, P. Zaslansky, C. Jud, M. Liebi, M. Guizar-Sicairos, and F. Pfeiffer, "Six-dimensional real and reciprocal space small-angle X-ray scattering tomography," *Nature* **527**(7578), 353–356 (2015).
36. M. Humar and S. H. Yun, "Intracellular microlasers," *Nat. Photonics* **9**(9), 572–576 (2015).

## 1. Introduction

Heart valve disease is a common condition affecting about 5 million people each year only in the US [1] and scales up to 13 million in European countries [2]. Due to its good performance and hemodynamics, biological prostheses are preferred over their mechanical counterparts for valve replacement in adults between 50 and 69 years [3]. One of the reasons for this limited age range is the high variability in performance of biological prostheses after 10 years of implantation that eventually leads to failure [4]. In general, valve failure is related to the degradation of the collagen network and thus deterioration of the mechanical properties of the valve [4]. Recent efforts in tissue engineering are focused on producing valves and organ

patches based on 3D printed technology [5]. However, a better understanding between the mechanical properties and the native structure of a tissue is still needed [6].

Collagen represents the building block of most connective tissue; it provides fundamental structural support and confers adequate mechanical properties to collagen-based tissues. This is particularly important for biological heart valve replacements because they are based on bovine pericardium (BP), a tissue mainly formed by collagen. Variations in the structural order and orientation of collagen lead to tissues with very different mechanical properties such as ligaments, skin, or corneal layers [7, 8]. In order to improve our understanding of a complex material such as collagen-based tissue, we need to know how the collagen structure confers the mechanical properties to the tissue. Amid the methods used for mechanical characterization, optical techniques provide non-contact means to determine features such as the preferred directions of collagen fibers under different loading conditions [9, 10]. This is relevant information for bioprosthetic heart valves because the mechanical response of the tissue used in the leaflets greatly depends on the fiber concentration, characteristics, and orientation [7,8]. Hence, advances in optical techniques, capable to resolve fiber attributes within the tissue are of great interest for these purposes.

Recently, we explored the use of Mueller matrix imaging (MMI), enhanced backscattering (EBS) and digital image correlation (DIC) to assess the mechanical behavior of BP [11]. The combination of these techniques yielded interesting results providing information about structural changes in the tissue during mechanical tests. Other approaches used for elucidating the relationship between the mechanical properties of collagen-based tissue and the orientation and concentration of its collagen network include the use of confocal microscopy coupled with biaxial loading [12], and the use of an ultra-stable optical trap with high-precision and high-bandwidth position detector [13]. Although all these techniques have showed promising results for structural analysis, they involve high-end facilities and elaborated experimental setups.

Random laser (RL) action is another promising technique with potential use in the characterization of complex materials. In short, RL action is the result from stimulated emission in which the feedback mechanism is provided by an ensemble of scatterers with random positions. RL action has been achieved using laser powders [14], liquid crystals [15], dielectric particles [16] and biological tissue [17, 18], to name a few. The idea behind using RL action for biological tissue characterization is supported by the fact that, according to RL theory, even small changes in the scattering ensemble may lead to dramatic changes in the characteristics of the RL emission [19, 20]. In other words, RL allows for mapping the changes in the microstructure to the spectral features (e.g., wavelength and laser threshold) of the laser emission. Here, we report on a different approach for the application of RL action obtained from BP impregnated with a laser dye. More specifically and in contrast with our previous work [21], we demonstrate spatially resolved RL intensity mapping (i.e., RL imaging) of collagen-based tissue simply by filtering the residual pump energy. Moreover, we show that along with image analysis of the RL emission, it is possible to obtain information regarding the longitudinal stress from individual collagen fibers during a tensile test. Furthermore, using DIC analysis, we have identified that the highest intensities in RL emission are related to the main directions of the applied force.

## 2. Materials and methods

### 2.1 Experimental setup

A mechanical testing device designed to perform tensile tests on thin and soft materials was used to stretch the bovine pericardium (BP) samples [21]. This mechanical “minitester” further incorporates optical elements to achieve RL emission from BP samples impregnated with a laser dye and to acquire information of the emitted laser light. As depicted schematically in Fig. 1, a Nd:YAG pulsed laser (New wave research, CA, USA) at 532 nm (20mJ max energy per pulse, 20Hz max frequency) was used to irradiate the tissue samples

with a spot diameter of approximately 0.5 cm. Sequences of images were acquired via a long working distance microscope objective (Mitutoyo Corp., Kawasaki, Japan) and a CCD camera (PixeLINK, ON, Canada), both arranged to register the beam coming out from the sample in the forward direction (red arrows in Fig. 1). Part of the light collected by the microscope objective was simultaneously analyzed with a high-resolution spectrometer (HR4000, Ocean optics, FL, USA) used for registering the spectral features of the RL emission. As shown in Fig. 1, a notch filter (Edmund optics, NJ, USA) was also used in order to block any residual pump from the sample. The addition of the notch filter (NF) avoided saturation of the camera and thereby allowed for acquiring images of the RL emission from the BP. This is important as the spatially resolved RL emission mapping is related with the efficiency of the RL cavities over the imaged area [22]. As discussed in the following sections, this spatially resolved RL mapping can readily provide information from individual collagen fibers during the tensile test.

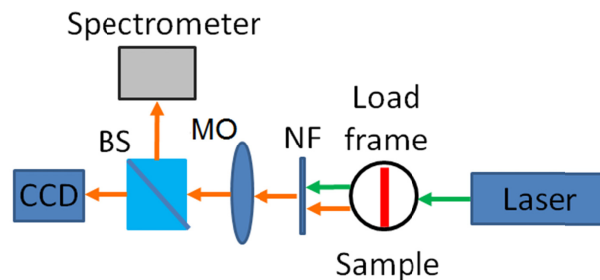


Fig. 1. Experimental setup: a CCD camera registers the RL emission from within the tissue samples. The setup includes a notch filter (NF), a beam splitter (BS), a laser, a  $5\times$  microscope objective (MO) and a spectrometer to register the spectral features of the emission

Conventional images were recorded using external white light illumination for subsequent processing using DIC. The mechanical tester, CCD camera, spectrometer and laser trigger were controlled and synchronized with a PC via a Virtual Instrument (VI) programmed in LabVIEW. The VI was set to start the test in a sequential manner; first, the sample was elongated in steps of  $200\ \mu\text{m}$  while simultaneously acquiring white light images as well as data such as applied force and displacement for subsequent mechanical analysis. The maximum loads reached in our experiments were within 7-8 MPa. In order to avoid spectral variations in the RL emission due to relaxation effects in the BP, the VI was set to pause for 4 minutes once the applied load reached a preset value. This relaxation time was determined experimentally through preliminary measurements showing that after 4 minutes, relaxation effects are negligible for RL analysis. After this pause, the Nd:YAG laser was triggered to launch 7 pulses with different energies. The pulse energies were set to probe pump energies below and above the RL threshold. For each pulse, the VI recorded images as well as the emission spectra from the BP sample. When this process was finished, the VI then restarted the loading procedure for data and image acquisition for different load magnitudes.

## 2.2 Sample preparation

For our experiments, pericardiums from 18 month-old calves were collected fresh from a local slaughterhouse. The sac was subsequently cross-linked with glutaraldehyde (GA); the fixation process was carried out during 24 hours at  $4^\circ\text{C}$ , using 0.5% GA in 0.1 M phosphate buffered saline solution with a pH of 7.4. This protocol has been customarily used to study the mechanical properties of bovine pericardium [7–9, 21, 23]. Next, the sac was washed in distilled water and subsequently cut with a special jig, according to the ASTM D1708 standard, to obtain samples in a dog bone shape (see Fig. 2(d)). All the samples were cut from the medial zone of the pericardium. Finally, the samples were immersed and stored in a

glycerin-Rhodamine 6G (R6G) solution until the experiments were performed. The optimum concentration of R6G in glycerin for these tests was determined in a separate experiment and was fixed at 0.8 g/l for all the experiments. Additionally, small slices of tissue were taken during the sample preparation processes. These were dehydrated in ethanol solutions, air dried at 60°C and then analyzed with a JEOL JSM-7600F scanning electron microscope (SEM). The SEM images shown in Fig. 2 depict a disordered fiber structure showing that collagen fibers maintain its naturally random disposition over the sample preparation process.

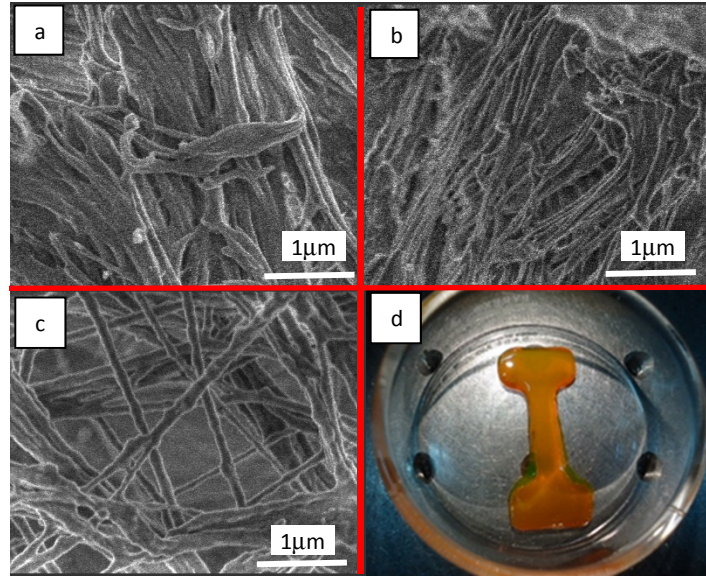


Fig. 2. SEM images of the tissue at different stages of the preparation protocol. a) Native pericardium; b) pericardium after fixation with GA; c) pericardium after glycerin immersion; d) image of a dog bone shape pericardium sample after fixation and immersion in the glycerin-R6G solution.

### 2.3 DIC analysis

Digital image correlation is a non-contact technique typically applied on full images to measure displacement/strain vector fields (DVF) on the surface of materials. With the series of acquired images during the mechanical tests, the DVFs  $\mathbf{u}_k(x_k, y_k)$  and  $\mathbf{v}_k(x_k, y_k)$  between pair of images were calculated using the Willert and Gharib algorithm [24]. Here  $\mathbf{u}$  and  $\mathbf{v}$  represent the displacement vectors in the  $x$  and  $y$  directions of the object or region of interest [25, 26]. The position coordinates in each image were represented by  $x$  and  $y$  and the sub index  $k$  indicated the corresponding object/region of interest, which is defined as an area of  $64 \times 64$  pixels. Hence, a full image was divided in subimages ( $64 \times 64$  pixels) used to perform the DIC analysis yielding the DVF throughout the full image for a given loading state. The in-plane strains in the sample were evaluated by minimizing the errors of a six parameters linear model (typically used in linear elasticity theory) and previously used in other materials, including bovine pericardium [25, 26]. This minimization yields the values for the normal strain in the  $x$  and  $y$  directions ( $\epsilon_x$  and  $\epsilon_y$ ), translation, shear strain ( $\epsilon_{xy}$ ), and in-plane rotation within the analyzed region of the sample [26].

### 3. Results and discussion

As customarily observed in RL experiments, spectral narrowing in the emission from the BP samples was observed as the pump energy was increased. After a given pump energy ( $\sim 5$  mJ), the full-width at half-maximum (FWHM) of the emission decreased to values of 5~7nm. Furthermore, for pump higher pump energies (up to 8 mJ), the output energy increased in a

linear fashion, as shown in the inset of Fig. 3. This threshold-like behavior, together with the spectral narrowing, are the characteristic features of RL emission [14, 17, 22]. Figure 3 shows a representative spectrum of the emission obtained while pumping the tissue samples (labeled as BP/R6G/Gly in Fig. 3). For comparison, Fig. 3 also shows the fluorescence spectrum of the R6G-glycerin solution obtained under similar pumping conditions (labeled as R6G/Gly in Fig. 3).

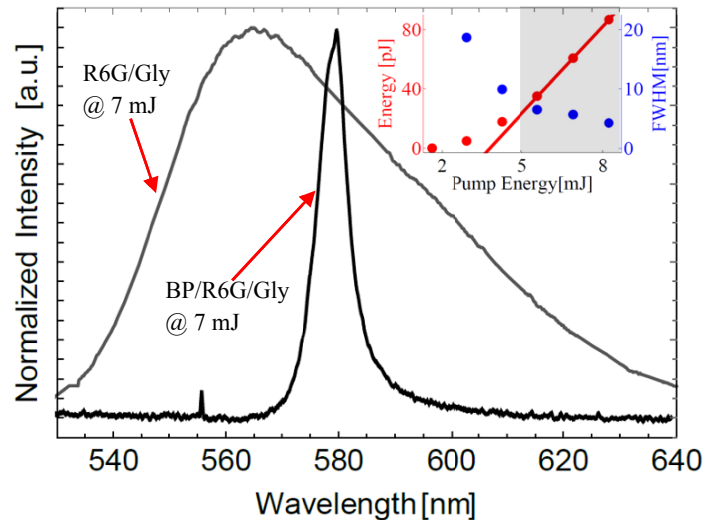


Fig. 3. Normalized spectra obtained from the glycerin-R6G solution (R6G/Gly) and typical RL emission from the tissue samples (BP/R6G/Gly); both spectra were obtained for a pump energy of 7 mJ. The inset shows the output energy from the RL sample as a function of pump energy (red data). Blue data correspond to the FWHM of the spectral emission obtained from the RL emission. A threshold of about 5 mJ was obtained for this sample and the FWHM decreased to 7 nm above the threshold energy.

The inset of Fig. 3 depicts the energy and FWHM of the emission as a function of pump energy. As the inset shows, the registered energy emitted from the sample increases linearly after a given value of pump energy. This threshold was determined to be around 5 mJ for all the studied samples, and further coincided with the pump energy at which the FWHM of the spectral emission decreased below 10 nm. The spectral narrowing together with a threshold behavior suggests that RL action indeed occurred within the tissue samples. Similar spectra were observed during the tensile test; however, in contrast to previous reports [21], we did not find a clear trend in the changes in the spectral features (i.e., FWHM, peak wavelength and energy) as a function of loading conditions. This is expected, as sample preparation will greatly influence the emission of RL; both, the threshold and spectral features have shown to vary under different experimental conditions, including the angle at which the laser emission is acquired [17–19, 27]. Optical characterization methods have previously demonstrated that the collagen fiber architecture is non-uniform and varies from region to region of the BP [9]. Clearly, the samples used for these experiments present a different mechanical behavior to that obtained in [21], as evidenced by the different spectral features of the RL emission obtained in our experiments.

Interestingly, the mapped intensity of the RL emission from the samples showed a good correlation with the DIC analysis. Figure 4 shows representative images for three different elongation conditions: the lowest stress induced during the test (elongation ratio ER = 0.001, 0.2 MPa) is depicted in row I, an intermediate stress condition is shown in row II (ER = 0.223, 4.7 MPa) and the highest strain attained during the test is shown in row III (ER = 0.330, 7.3 MPa). Figure 4 further shows a set of white light images of a sample during a typical tensile test (left column) and its corresponding RL intensity map (right column). The

pump energy for these images was 8 mJ, well above the threshold value ( $\sim 5$  mJ, see inset of Fig. 3). For direct comparison with the intensity maps, the displacement vector fields obtained by DIC for each deformation condition are shown as white arrows in the left column. Upon comparing both columns, it can be seen that the high RL intensity zones match most of the superficial fibers observed in the images (shown in Fig. 4 with black ovals). This indicates that most of the RL emission originates from within individual fibers, and not from the sections with higher fiber density in the sample. This was somewhat unexpected given that RL emission relies on a high concentration of scatterers: intuitively, one would expect increased scattering effects within the cross-linked sites for collagen treated tissue. However, our experimental results suggest that individual fibers can sustain RL emission. Because they are made of microfibers and fibrils in a complex and disordered arrangement [7, 9], collagen fibers may provide multiple scattering effects needed to achieve RL action. Moreover, RL action can be sustained inside individual collagen fibers and several volumetric modes may arise in each collagen fiber. A rough estimation on the number of modes in a collagen fiber can be computed using the Rayleigh–Jeans formula [28]:

$$N = 4\pi \frac{V}{\lambda_{peak}^4} FWHM \quad (1)$$

In Eq. (1),  $FWHM$  is the spectral width of the emission,  $\lambda_{peak}$  is the central wavelength of the emission, and  $V$  is the pumped volume of the gain medium. Considering a single pumped fiber with a diameter of 20  $\mu\text{m}$  and 10 mm long, which are representative dimensions of the fibers shown in Fig. 4, and taking into account the spectral features of the RL emission (see Fig. 3), the number of modes would be in the order of  $1 \times 10^6$ . All of these modes, along with those from the rest of the pumped collagen fibers, would contribute to the combined laser emission registered in our experiments. The mode spacing within the spectral width of the RL emission ( $\sim 10$  nm) would therefore be extremely small, making impossible the identification of each lasing mode with the current experimental setup.

The intensity map of the first row in Fig. 4 shows that initially, only a few spots of high RL intensity (red-orange colored) are obtained from the sample. As the stress increased during the test, more spots with high intensity were observed. Given that the pump energy was held constant, this behavior suggests that the RL becomes more efficient with the applied stress. During elongation, the fibers rearrange to minimize the mechanical energy induced by the stress condition [7]. This in turn generates zones with an increased concentration of scatterers, thus locally increasing the RL intensity. It is evident from the figures that some of the imaged fibers experience an increase in RL intensity. In general, the images obtained under increased elongation conditions showed higher laser intensity over the imaged area.

A relationship between the RL and DIC analysis can be made upon comparing the displacement vector field (DVF) with the RL imaging. For an ER = 0.22 (Fig. 4, row II), DIC analysis yields a well-defined hyperbolic structure. This is a characteristic feature of a fiber ensemble undergoing uniaxial tension [25, 26]. The fiber with the highest RL intensity seems to align along the direction of the tension axis of the hyperbolic pattern. For the maximum stress induced during the test (ER = 0.33, Fig. 4, row III), the fiber exhibiting highest intensity emission matches not only the direction, but also the position of the vertical component of the DVF. Notice however that fiber populations with specific orientations will be realigned differently when undergoing tensile tests [9]. Hence, different behaviors for the RL emission can be expected for fibers with different alignments.

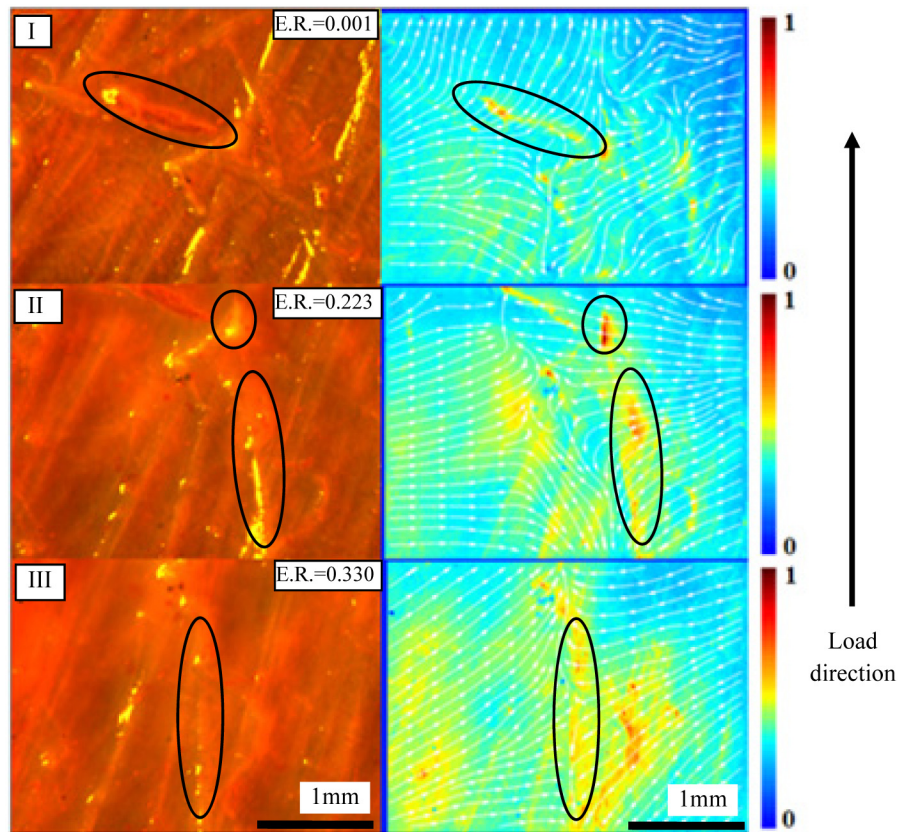


Fig. 4. Left column: white light images of the tissue samples. Right column: intensity maps of the RL emission and their corresponding DVF. The color scale was normalized to the maximum intensity value found during the test. Each row corresponds to a different stress condition (I: ER = 0.001, 0.2MPa; II: ER = 0.223, 4.7MPa; III: ER = 0.330, 7.3MPa). Black ovals show some of the superficial fibers matching the high intensity zones in the RL intensity mapping. The black arrow in the right indicates the direction of the applied load.

To illustrate the effect of fiber orientation during the tensile test we selected another sample with a different fiber distribution. Specifically, the RL intensity of two fibers within the field of view was registered during the test. We selected the fibers that showed the most orthogonal orientations with respect to each other within the image (see Fig. 5(a)). These were chosen because they represent cases in which the fiber is either parallel or perpendicular to the applied stress. By tracking the position of these fibers individually, the corresponding RL intensity was analyzed for each elongation condition. Notice that because of the different orientations of each fiber, elongation will induce different local stresses on each of them

Initially, one of the tracked fibers had an almost horizontal orientation (labeled as HF in Fig. 5(a)) with respect of the loading direction, and is thus oriented perpendicularly to the applied stress. In contrast, the other fiber selected for tracking had initially an oblique orientation (about 45° and labeled OF in Fig. 5(a)). While this fiber gradually realigned along the direction of the applied stress axis during elongation (see Fig. 5(c)), the orthogonal fiber showed less variation in its orientation (see Fig. 5(b)). Notice also that while for fiber OF the RL intensity increases with elongation, the corresponding intensity for the HF fiber decreases (see insets in Fig. 5(b) and Fig. 5(c)). This trend is further verified by plotting the variations in mean pixel intensity during elongation for each fiber (see plots in Fig. 5(b) and Fig. 5(c)). The difference in mean intensity pixel ( $\Delta\text{Mean pixel intensity}$ ) shown in the plots of Fig. 5 is defined as  $(\bar{I}_0 - \bar{I}_n) \times 100$  where  $\bar{I}_0$  correspond to the mean intensity per pixel of a fiber at the

lowest stress induced during the test and  $\bar{I}_n$  correspond to the mean intensity per pixel of the fiber for a given elongation ratio during the test. Clearly, the stress conditions and hence the RL emission are both dependent on the orientation of the fibers.

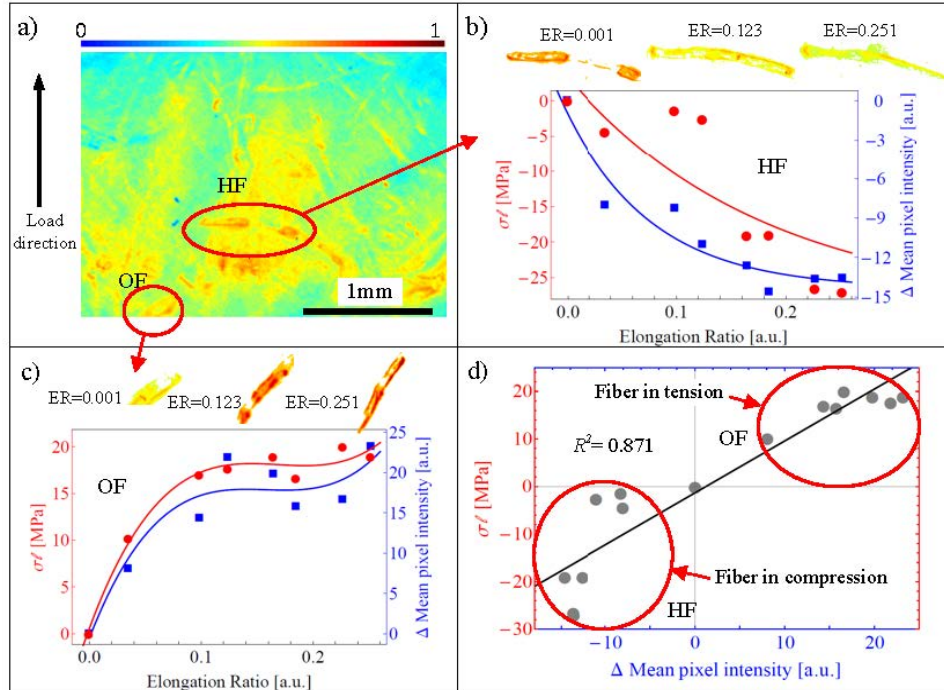


Fig. 5. Fiber tracking during the mechanical test. a) intensity map of the RL emission for the initial condition of the test. The ovals indicate the two fibers selected for tracking during the test (labeled HF and OF) and the black arrow indicate the direction of the applied load. b) and c) difference in mean pixel intensity obtained from the intensity maps and the longitudinal stress as function of the ER for each selected fiber. Some of the corresponding intensity maps of the fibers are shown as insets above the plots. d) longitudinal stress as a function of difference in mean intensity pixel for the two selected fibers. The black solid line corresponds to a least square fitting.

A first approximation to correlate the RL intensity and the stress induced in the individual fibers may be derived from the in-plane strain equations from the generalized Hooke's law. Hence, the longitudinal and transverse strains ( $\varepsilon_l$ ,  $\varepsilon_t$ ) for each fiber can be obtained as:

$$\begin{aligned}\varepsilon_l &= \frac{1}{E}(\sigma_l - \nu\sigma_t) \\ \varepsilon_t &= \frac{1}{E}(\sigma_t - \nu\sigma_l)\end{aligned}\quad (2)$$

These expressions are only valid under infinitesimal strain conditions and thus may be used for pair of images acquired under small deformation conditions [29]. Both strains can be calculated from the white light images by measuring changes in length and width of the selected fibers. The Young modulus  $E$  was considered constant during the test and was calculated from the stress-elongation ratio curve as in [21]. The Poisson ratio  $\nu$  was assumed to be equal to 0.5 as commonly done for elastomeric materials. Under these considerations we can obtain the stresses along the longitudinal and transverse axes ( $\sigma_l$ ,  $\sigma_t$ ) from Eq. (2). The longitudinal stress as a function of the elongation ratio for each fiber is shown in Fig. 5(b) and Fig. 5(c), along with the corresponding RL intensity. As the elongation increases, the

longitudinal stress for the OF fiber increases accordingly, while the longitudinal stress for the HF fiber decreases. Our results indicate that these perpendicular fibers experience opposite stresses (tension and compression), in agreement with the Poisson ratio assumed for the calculations and with previous reports for similar tissues [9, 25].

Remarkably, the trend of the curves shown in Fig. 5(b) and Fig. 5(c) is similar, suggesting that the RL intensity may correlate to the induced stresses. This was verified upon plotting the longitudinal stress for the selected fibers calculated from Eq. (2) against the difference in mean intensity pixel obtained from the RL emission (see Fig. 5(d)). A least square fitting yields a correlation parameter  $R^2 = 0.87$ . Notice that the plot represents both, the tension and compression experienced by the OF and HF fibers, respectively. Notice also that the only difference between these fibers is their relative orientation with respect to the stress axis, and yet the RL intensity variation is very different. A possible scenario explaining this optomechanical behavior is a local change in the scatterer density inside the fibers, induced by a tensional-compressional stress. When a fiber is subjected to tensional stress, its inner structure tends to pile into smaller diameters [7]; this may lead to an increase in the number of scatterers per unit volume thereby increasing the scattering force of the random medium [22]. Conversely, the compressive stress may decrease the scattering force of an individual fiber owing to an increase in fiber diameters. Even though the small change in the microstructure of the collagen fibers is not detectable by white light imaging or conventional mechanical tests, the RL effect seems to be sensitive to such changes because an adequate variation of scatterer density can lead to drastic changes in the amount of RL emission. Although the nature of the feedback mechanisms in RL is still controversial, it has been shown that the amount of scattering in a disordered medium can determine their regime of operation [30]. In this sense, from the perspective of the mechanical tests performed in our experiments, the RL intensity and the stress applied to individual fibers seem to be related by the modification of the inner structure of the fibers.

The correlation between the RL intensity and the individual stress applied on each fiber may represent a simpler means to understand collagen hierarchy. Recently, nonlinear optical effects such as multiphoton photon absorption [31] and second harmonic generation [32] have improved the assessment of fiber structure in collagen-based tissues under mechanical loads. Similarly, birefringence measurements by means of polarized second harmonic generation (p-SHG) have provided new insights on the orientation of the collagen fibers of tendon tissue under mechanical stretching [33]. As demonstrated with p-SHG, the imposed strain within the tissue tends to align the collagen fibers increasing the anisotropy, which in turns translates in an increase in birefringence. Our results are in good agreement with these findings because RL intensity depends on the density of scatterers per unit of volume (in our case fibrils per unit of volume). Since fibril alignment will vary under different loading conditions, it is reasonable to expect that the RL intensity will vary accordingly. In particular, our results suggest that fiber elongation leads to an increase scattering, whereas fiber compression will decrease it. Studies about deformation of collagen-based tissues at the nano-scale have been typically based on x-ray spectroscopy [7] and techniques such as wide-angle x-ray diffraction (WAXD) [34] and small angle x-ray scattering (SAXS) [35]. These approaches require elaborated setups and expensive facilities such as a synchrotron source, an enclosed fluid chamber with transparent windows and low noise x-ray detectors. Compared to WAXD and SAXS, RL emission imaging would allow probing the fibril hierarchy in a simple and cost-effective manner. Recent advances on hyperspectral imaging may further increase the reach of RL intensity analysis during mechanical tests [36].

#### 4. Conclusions

We have demonstrated the application of laser emission obtained from BP tissue to obtain spatially resolved RL intensity mapping. This RL imaging technique offers a novel means to provide information of individual fibers within collagen-based tissue samples. In particular,

the variations on the RL intensity from each fiber can be correlated to the longitudinal stresses experienced by the fibers under uniaxial tension tests. For our experimental conditions, we were able to identify that RL emission is generated from within the collagen fibers of the tissue. Some of the implications of this statement are that for each collagen fiber pumped, a myriad of modes can be excited within the fiber. We believe that the information obtained with this technique may represent a simple means to obtain information about the structural features of complex materials such as collagen-based tissue.

**Funding**

DGAPA-UNAM (PAPIIT IT101215 and IN104118); UC-MEXUS CONACYT (Postdoctoral fellowship 2017-2018).

**Acknowledgments**

JHC acknowledges support from PASPA-DGAPA-UNAM and from Conacyt during his sabbatical at UCR.

Technical support from Dr. Omar Novelo for acquiring the SEM images is duly appreciated.

**Disclosures**

The authors declare that there are no conflicts of interest related to this article.